EES Catalysis

PAPER

View Article Online
View Journal

Cite this: DOI: 10.1039/d6ey00096g

Electrochemical amorphous-to-1T-phase reconfiguration of Ru–W bimetallic sulfide for sustainable hydrogen evolution

Jingchun Wang, †[a] Xiao Yu,†[b] Yan Sun,*[a] Yipeng Zang,[c] Xujiang Yu,[d] Haolan Tao,*[b] Cheng Lian *[b] and Huibin Qiu *[a]

Received 5th May 2026,
Accepted 7th May 2026

DOI: 10.1039/d6ey00096g

rsc.li/eescatalysis

Electrochemical reconfiguration of amorphous metallic materials offers exceptional opportunities for catalyst design. Here, we demonstrate a distinctive reconfiguration route toward highly active crystalline 1T-phase in amorphous Ru–W bimetallic sulfide. A micellar film-mediated strategy is developed to facilely fabricate large-area mesoporous films of the amorphous composite, involving sequential accumulation and association of Ru^{3+} and WS_4^{2-} precursors through hierarchical "pyridyl–Ru^{3+}–WS_4^{2-}" coordination, followed by crystallization-retarding pyrolysis. The resulting catalyst reveals appealing hydrogen evolution performance, with a low initial overpotential of 11 mV at 10 mA cm^{-2} and high sustainability at 1.0 A cm^{-2} over 1600 h. Notably, sustained electrochemical stimuli trigger a distinctive amorphous-to-crystalline reconfiguration, gradually generating crystalline Ru–W bimetallic sulfide with a metastable 1T-phase. This substantially endows the catalyst with a remarkable long-term stability while further enhancing the catalytic activity (overpotential of only 4 mV at 10 mA cm^{-2}). Theoretical calculations reveal an electrochemical-dependent structural reorganization process, where external electron injection triggers charge redistribution that drives the atomic rearrangement, while the sulfur-bridged structure promotes efficient cooperative charge transfer and ensures the structural robustness of the metastable 1T-phase during the reconfiguration.

Broader context

Electrochemical reconstruction of amorphous metallic materials presents an exceptional opportunity for catalyst design. However, the transformation into highly active metastable crystalline phases with unique electronic structures is rarely discovered. Here, we develop a micellar film-mediated strategy to facilely fabricate large-area mesoporous films of amorphous Ru–W bimetallic composite, involving hierarchical "pyridyl–Ru^{3+}–WS_4^{2-}" coordination and crystallization-retarding pyrolysis. Notably, the amorphous Ru–W bimetallic sulfide exhibits an unconventional reconfiguration from amorphous to crystalline 1T-phase during the electrochemical hydrogen evolution reaction. Theoretical calculations reveal that this transformation originates from electrochemical injection of electrons, which induces interatomic charge redistribution to establish a new coordination environment, thereby driving the atomic rearrangement. In this process, the bridged sulfur provides a critical and efficient synergistic charge transfer pathway that simultaneously ensures the structural stability of the 1T-phase. Taking advantage of the persistent electrochemical reorganization into the highly active 1T-phase, such an amorphous catalyst exhibits outstanding long-term stability and superior electrocatalytic activity for hydrogen evolution. In general, the open and coordinative soft environment of the micellar film provides an innovative platform for the tunable synthesis of functional amorphous composites and the subsequent phase engineering toward highly active electrocatalysts for sustainable energy conversion technologies.

[a] State Key Laboratory of Synergistic Chem-Bio Synthesis, School of Chemistry and Chemical Engineering, Frontiers Science Center for Transformative Molecules, State Key Laboratory of Micro-Nano Engineering Science, Shanghai Jiao Tong University, Shanghai 200240, China. E-mail: syzzyy07@sjtu.edu.cn, hbqiu@sjtu.edu.cn
[b] State Key Laboratory of Chemical Engineering and Low-Carbon Technology, School of Chemistry and Molecular Engineering, East China University of Science and Technology, Shanghai 200237, China. E-mail: haolan_tao@ecust.edu.cn, liancheng@ecust.edu.cn
[c] State Key Laboratory of Catalysis, Dalian Institute of Chemical Physics, Chinese Academy of Sciences, Dalian 116023, China
[d] State Key Laboratory of Metal Matrix Composites, School of Materials Science and Engineering, Zhangjiang Institute for Advanced Study, Shanghai Jiao Tong University, Shanghai 200240, China
† J. Wang and X. Yu contributed equally to this work.

Introduction

Amorphous metallic materials inherently possess a high density of structural defects, unsaturated coordination sites, and tunable local bonding environments.[1–6] Such features effectively reduce the reaction energy barrier and optimize the mass transport pathways, leading to frontier catalytic systems for critical electrochemical reactions, including hydrogen evolution and carbon dioxide reductions.[7–14] Notably, metastable characteristics render them highly susceptible to dynamic structural evolution under electrochemical conditions, presenting both opportunities for performance modulation and challenges for mechanistic understanding of electrochemical reconfiguration.[15,16] Utilizing this evolution to rationally generate active species has emerged as a critical strategy to construct efficient and stable catalytic systems.[17–20] To date, the reconfiguration of amorphous materials predominantly yields amorphous-to-amorphous transitions, occasionally accompanied by nanoscale surface/local crystallization/passivation or phase separation induced by elemental leaching[21–28] (Fig. 1a). The resulting crystalline products (*e.g.*, metals, oxides, hydroxides,[29–33] *etc.*) are typically thermodynamically stable, while metastable phases with special electronic structures and high activity are rarely discovered.

Metal sulfides (*e.g.*, WS_2, MoS_2, *etc.*) with unique/tunable electronic structures and abundant active sites create favorable conditions for various catalytic processes.[34–38] Particularly, the thermodynamically metastable 1T-phase exhibits exceptional electrochemical activity due to its metallic conductivity, octahedral coordination, and extensible interlayer spacing that facilitates charge transfer.[39] It can be controllably prepared with various approaches, including direct synthesis (*e.g.*, ion intercalation, chemical vapor deposition, *etc.*)[40–44] and external field-controlled transformations (*e.g.*, strain, plasma induction, *etc.*).[45–49] However, the generation of 1T-phase by direct electrochemical reconfiguration from amorphous materials remains unexplored. The amorphous metal sulfides prepared by current methods (*e.g.*, wet-chemical method, chemical vapor deposition)[50–52] have not yet been employed as critical precursors for the electrochemical reconfiguration to generate the 1T-phase.

Herein, we develop a polystyrene-*b*-poly(2-vinylpyridine) (PS-*b*-P2VP) block copolymer micellar film system to mediate the uniform construction of an amorphous mesoporous bimetallic sulfide film (Fig. 1b). Specifically, the micellar film enables the sequential accumulation of Ru^{3+} and WS_4^{2-} ions through a hierarchical "pyridyl–Ru^{3+}–WS_4^{2-}" coordination route. Subsequently, *in situ* confined pyrolysis of such metal species-accumulated micellar film directly induces the formation of amorphous Ru–W bimetallic sulfide (denoted as RuWS). In particular, the micellar film mitigates excessive co-precipitation of metal species and retards the crystallization kinetics induced by high temperatures, ensuring the preservation of amorphous structures with a sulfur-bridged coordination configuration. Notably, during the electrocatalytic reaction, the amorphous film gradually transforms to crystalline Ru–W bimetallic sulfide with a metastable 1T-phase (Fig. 1b). Theoretical calculations further demonstrate that the electrochemical injection of electrons triggers the amorphous-to-crystalline reconfiguration, where the sulfur-bridged structure effectively balances the

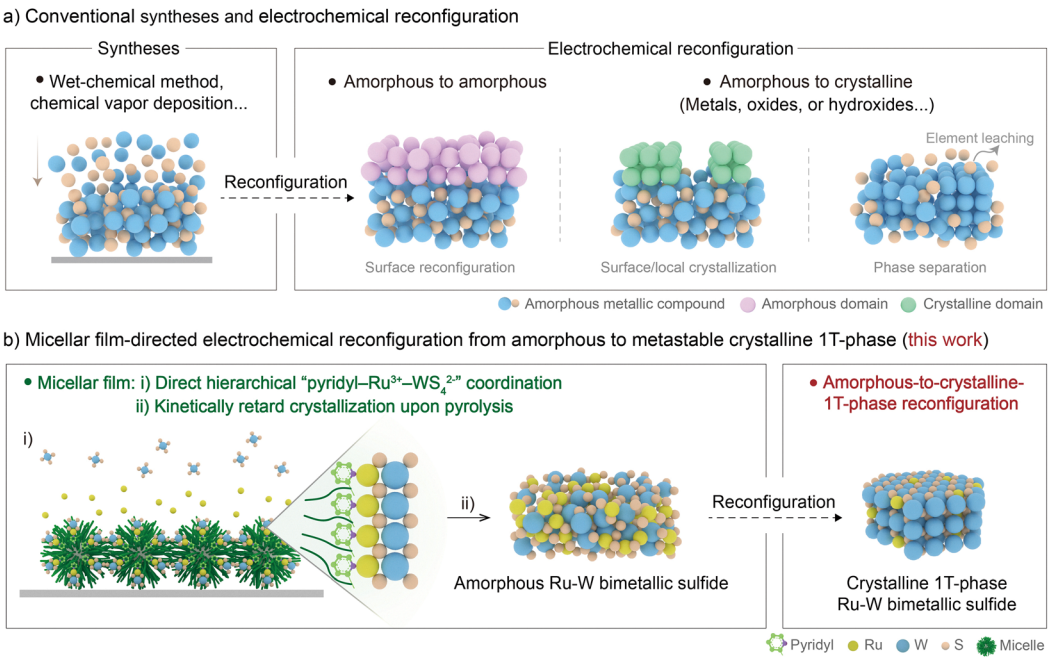

Fig. 1 Electrochemical reconfiguration. (a) Traditional syntheses and electrochemical reconfiguration of amorphous materials. (b) Micellar film-mediated formation of amorphous bimetallic sulfide *via* hierarchical coordination and electrochemical conversion into crystalline bimetallic sulfide with a metastable 1T-phase.

electron redistribution between various atoms through rapid charge transfer and efficiently handles the structural strain to sustain the metastable crystalline phase.

Results and discussion

Fabrication of RuWS-accumulated PS-*b*-P2VP micellar film

Micellar films were prepared on desired substrates *via* direct drop-casting and rapid solvent evaporation of a solution of PS-*b*-P2VP unimers[53] (Fig. 2a). Such micellar film solely consisted of a large number of tightly stacked spherical micelles (with a PS core and a P2VP corona) (Fig. S1). Upon treatment in a KOH solution, the micellar film can be separated from the substrate to form a large-area free-standing film (Fig. S2), implying its integral structure and remarkable mechanical robustness. Subsequently, the micellar film was immersed in a solution of $RuCl_3$ in ethanol. While the morphology remained nearly intact, the color of the micellar film gradually became yellow (Fig. 2b), indicating the capture of Ru^{3+} in the P2VP corona of the spherical micelles (Fig. S3), mainly through coordination. Further, upon immersing the Ru^{3+}-accumulated micellar film into a solution of $(NH_4)_2WS_4$ in a 1 : 1 (v/v) mixture of isopropanol and water, a brown film was obtained (Fig. 2b). Scanning electron microscopy (SEM) and transmission electron microscopy (TEM) images showed that after the sequential loading of

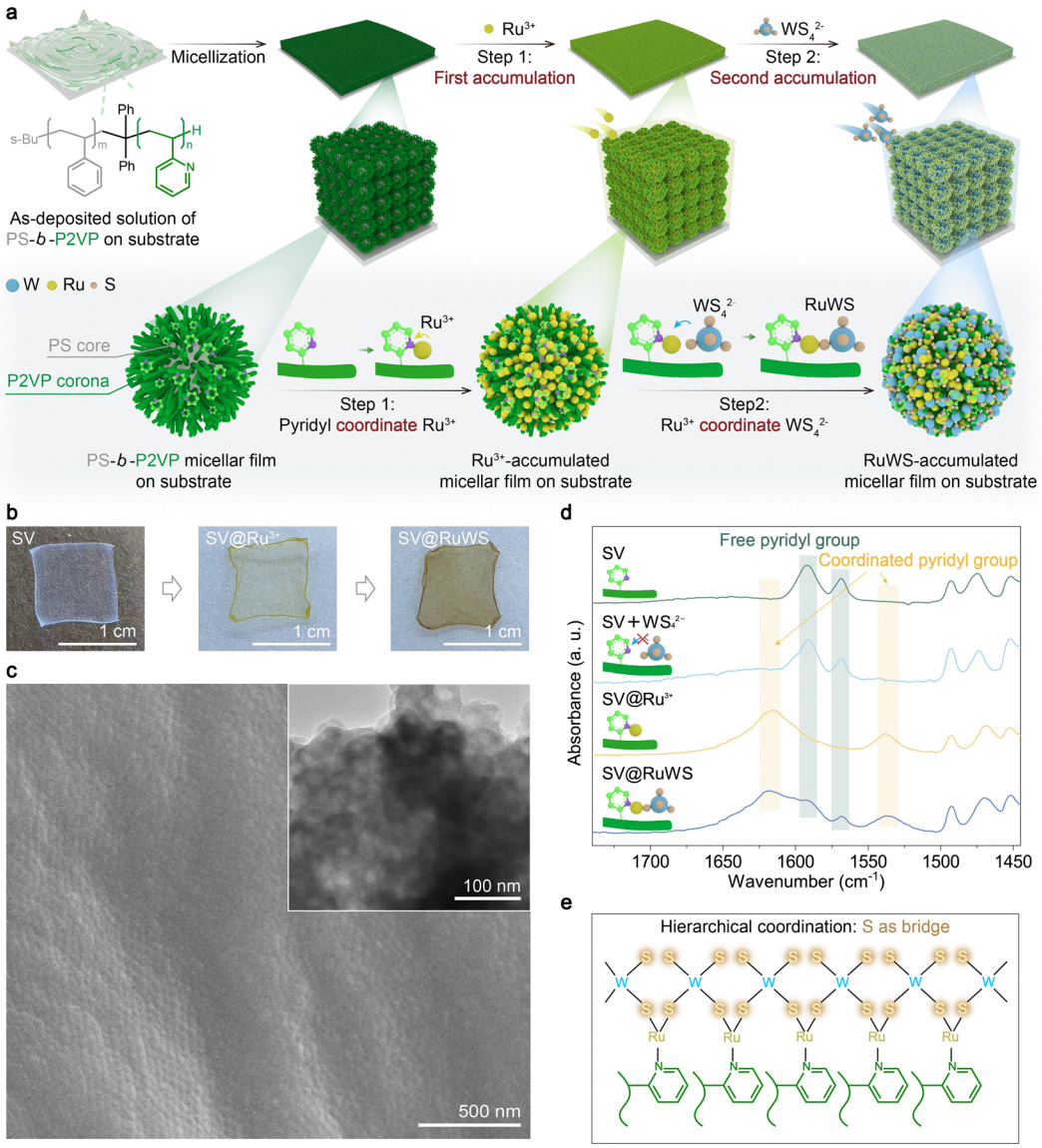

Fig. 2 Micellar film-directed sequential accumulation of Ru^{3+} and WS_4^{2-} *via* hierarchical coordination. (a) Schematic illustration of the preparation of Ru–W bimetallic sulfide-accumulated PS-*b*-P2VP micellar film. (b) Photographs of a free-standing micellar film and that after accumulation of Ru^{3+} ions (denoted as SV@Ru^{3+}) and successive accumulation of both Ru^{3+} and WS_4^{2-} ions (denoted as SV@RuWS). (c) SEM and TEM (inset) images of RuWS-accumulated micellar film. (d) FT-IR spectra of PS-*b*-P2VP micellar film, PS-*b*-P2VP micellar film after immersing in a solution of WS_4^{2-} ions in ethanol, Ru^{3+} ion-accumulated PS-*b*-P2VP micellar film, and RuWS-accumulated PS-*b*-P2VP micellar film (denoted as SV, SV + WS_4^{2-}, SV@Ru^{3+}, and SV@RuWS, respectively). (e) Schematic illustration of the hierarchical coordination.

Ru^{3+} and WS_4^{2-} the micellar film preserved the homogeneous morphology and the internal dense stacking of spherical micelles (Fig. 2c and Fig. S4a, b). High-resolution TEM (HRTEM) images and fast Fourier transform (FFT) pattern (Fig. S4c and d) both demonstrated the absence of crystalline component, which is consistent with the results of X-ray diffraction (XRD) (Fig. S5). High-angle annular dark field scanning TEM (HAADF-STEM) images and elemental mapping further confirmed the relatively homogenous distribution of Ru, W, and S elements (Fig. S4e).

To elucidate the association patterns among pyridyl groups on P2VP, Ru^{3+} and WS_4^{2-}, a factorial cross-comparison analysis was systematically conducted. Fourier transform infrared (FT-IR) spectra showed that while the micellar film barely associated with the WS_4^{2-} ions, it revealed a remarkable association with the Ru^{3+} ions, mainly involving coordination interactions with the pyridyl groups (Fig. 2d). Notably, after the secondary addition of WS_4^{2-} ions, the micellar film revealed attenuated signals for the coordinated pyridyl groups, while the peaks for the free pyridyl groups recovered. It appeared that the introduction of WS_4^{2-} ions triggered a slight dissociation of Ru^{3+} from the pyridyl groups. On the other hand, the direct mixing of Ru^{3+} and WS_4^{2-} in the absence of micellar film yielded irregular non-mesostructured RuWS powder (Fig. S6) and UV-visible absorption spectra showed a strong interaction between Ru^{3+} and WS_4^{2-} (Fig. S7). Apparently, the sequential accumulation of Ru^{3+} and WS_4^{2-} ions facilitated a hierarchical coordination of "pyridyl–Ru^{3+}–WS_4^{2-}" (Fig. 2e) in the micellar film, where S atoms bridge the pyridyl groups, Ru^{3+} and WS_4^{2-}. X-ray photoelectron spectroscopy (XPS) results for Ru 3p, W 4f and S 2p revealed valence states of Ru at +3, W at +6, and S at −2, respectively, the same as for the $RuCl_3$ and $(NH_4)_2WS_4$ precursors (Fig. S8).

Fabrication of amorphous mesoporous bimetallic sulfide film

The RuWS-accumulated PS-*b*-P2VP micellar film on a specific substrate was subjected to pyrolysis under nitrogen at 600 °C to remove the micellar scaffold (Fig. 3a). This immediately generated a mesoporous film featuring a large-scale integration of uniformly sized spherical cavities and a homogeneous porous surface (Fig. 3b and Fig. S9). TEM images showed that the resulting film possessed well-defined mesopores with an average diameter of *ca.* 28.1 nm (Fig. 3b and Fig. S10). In particular, the hierarchical coordination structures provided critical rigid support and constraint for the mesopores.[53] Nitrogen sorption measurements further confirmed such mesoporous structure (Fig. S11). HRTEM, aberration-corrected HAADF-STEM (AC-HAADF-STEM) and corresponding FFT images (Fig. 3c and Fig. S12, S13) showed that the mesoporous film generally possessed an amorphous framework, with randomly arranged atoms. The XRD pattern also demonstrated the amorphous nature (Fig. S14). On the other hand, HAADF-STEM and element mapping images confirmed the co-existence of Ru, W, and S elements and revealed their uniform distribution throughout the film (Fig. 3d). Additionally, trace carbon and nitrogen residues were present in this film (Fig. S15). X-ray absorption near-edge structure (XANES) spectra at the Ru K-edge revealed slightly lower absorption edges for the pyrolyzed sample (Fig. S16a). Meanwhile, the intensity of white line at the W L_3-edge in XANES spectra was decreased (Fig. S16b). Such results suggested the lower valence states for both Ru and W,[54,55] aligning well with the corresponding XPS results (Fig. S17). The corresponding Fourier-transformed extended X-ray absorption fine structure (EXAFS) spectra at the W L_3-edge and Ru K-edge revealed characteristic peaks at 1.30 and 1.71 Å for W–S and Ru–S coordination, respectively (Fig. 3e and f). Notably, no significant correlation signal was observed between the metal atoms. It appeared that the sulfur atoms bridged the Ru and W atoms, facilitating the generation of the amorphous mesoporous RuWS film. This was consistent with the coordination structure of "pyridyl–Ru^{3+}–WS_4^{2-}" in the precursor.

To gain deeper insights, the evolution of non-mesostructured RuWS powder and RuWS-accumulated micellar film in the pyrolysis process performed at gradually increasing temperatures was carefully examined (Fig. S18–S31). For non-mesostructured RuWS powder, crystalline domains began to appear upon pyrolysis at 400 °C and dominated at higher temperatures (Fig. S18–S22). The highly crystalline powder formed at 600 °C solely consisted of isolated Ru and WS_2 phases (Fig. S22). On the contrary, for RuWS-accumulated micellar film, the amorphous mesoporous architecture was retained well even after pyrolysis at 600 °C (Fig. 3 and Fig. S23–S27), before the generation of homogeneously distributed tiny crystalline nanoparticles at 700 °C and larger crystalline domains at higher temperatures (Fig. S28–S31). It can be anticipated that the spatially confined coordination in the micellar film reduced the collision of Ru, W, and S species, consequently retarding the crystal growth rate within a defined thermal regime. Similarly, the treatment of Mo-based materials yielded mesoporous amorphous Ru-Mo bimetallic sulfide (denoted as RuMoS) film (Fig. S32).

Electrocatalytic performance of amorphous mesoporous RuWS film

Subsequently, the hydrogen evolution reaction (HER) activity of amorphous mesoporous RuWS film on carbon cloth was evaluated using a typical three-electrode system in 1.0 M KOH (Fig. 4 and Fig. S33). The amorphous mesoporous RuWS film formed at 600 °C exhibited the optimal performance (Fig. S34) and hence it was predominantly used for further investigation. Commercial Pt/C, crystalline WS_2 powder (derived from pyrolysis of $(NH_4)_2WS_4$ powder at 600 °C; Fig. S35), and crystalline Ru/WS_2 powder (derived from pyrolysis of non-mesostructured RuWS powder at 600 °C) were selected as the control samples. The amorphous mesoporous RuWS film revealed remarkably lower overpotentials of 11 mV at 10 mA cm^{-2} and 48 mV at 100 mA cm^{-2} compared with commercial Pt/C (43 and 273 mV), crystalline WS_2 powder (60 and 316 mV) and crystalline Ru/WS_2 powder (26 and 186 mV) (Fig. 4a and Fig. S36). In addition, at a high current density of 1000 mA cm^{-2}, the amorphous mesoporous RuWS film also revealed a relatively low overpotential of 130 mV and a Tafel slope of 23.2 mV dec^{-1} (Fig. 4a and b),

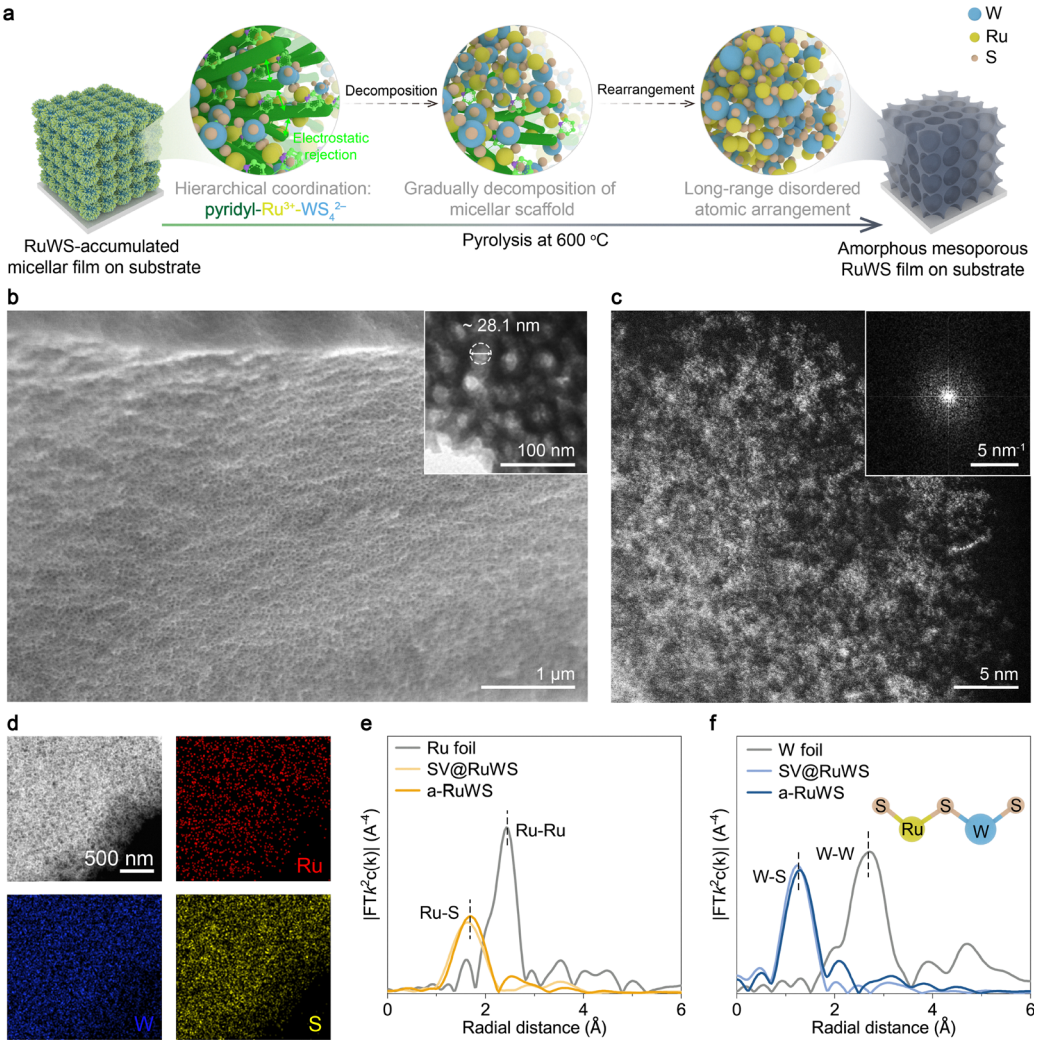

Fig. 3 Micellar film-directed formation of amorphous mesoporous RuWS film. (a) Schematic illustration of the conversion of RuWS-accumulated PS-*b*-P2VP micellar film into mesoporous film of amorphous RuWS upon pyrolysis at 600 °C. (b) SEM and TEM (inset) images, (c) AC-HAADF-STEM and corresponding FFT with characteristic weak diffusion ring (inset) images, and (d) HAADF-STEM and elemental mapping images of amorphous mesoporous RuWS film. (e) and (f) EXAFS spectra at (e) Ru K-edge and (f) W L_3-edge of amorphous mesoporous RuWS film and RuWS-accumulated micellar film (denoted as a-RuWS and SV@RuWS).

indicating a superior HER electrocatalytic activity toward industrial applications. Nyquist plots showed that the amorphous mesoporous RuWS film exhibited a smaller semicircular diameter in electrochemical impedance spectroscopy (EIS) compared with other samples, suggesting a lower charge transfer resistance (Fig. S37 and S38). The electrochemical double-layer capacitance (C_{dl}) (134.5 mF cm^{-2}) of the amorphous mesoporous RuWS film was significantly higher than that of other samples, implying an increased density of active sites (Fig. 4c and Fig. S39). Moreover, the amorphous mesoporous RuWS film also possessed an excellent hydrophilicity that would facilitate an electrocatalytic reaction (Fig. S40). Overall, the self-supported amorphous mesoporous film architecture was more conducive to active site exposure and mass/electron transfer, leading to a considerable improvement of HER activity (Fig. 4d).

Chronoamperometry tests were conducted at current densities of 10, 100 and 1000 mA cm^{-2} to evaluate the stability of amorphous mesoporous RuWS film (Fig. 4e and Fig. S41). After 100 h of stability testing, negligible current decays with minimal fluctuations were observed at current densities of 10 and 100 mA cm^{-2} (Fig. S41). Notably, the sample displayed a continuous operation at a current density of 1000 mA cm^{-2} for over 1600 h in an alkaline electrolyte with negligible metal leaching confirmed by ICP-OES, demonstrating an exceptional long-term stability (Fig. 4e and Table S1). Surprisingly, the post-test sample revealed an even lower overpotential of only 4 mV at 10 mA cm^{-2} and a Tafel slope of 10.2 mV dec^{-1} (Fig. 4f and Fig. S42), indicating the emergence of obviously enhanced catalytic activity and kinetics. EIS showed that the post-test sample also exhibited a decreased charge transfer resistance and thus a more efficient electron transfer capability (Fig. 4g). These features were extremely appealing compared with previously reported amorphous/Ru-based electrocatalysts in alkaline media (Fig. 4h and Table S2). An anion-exchange

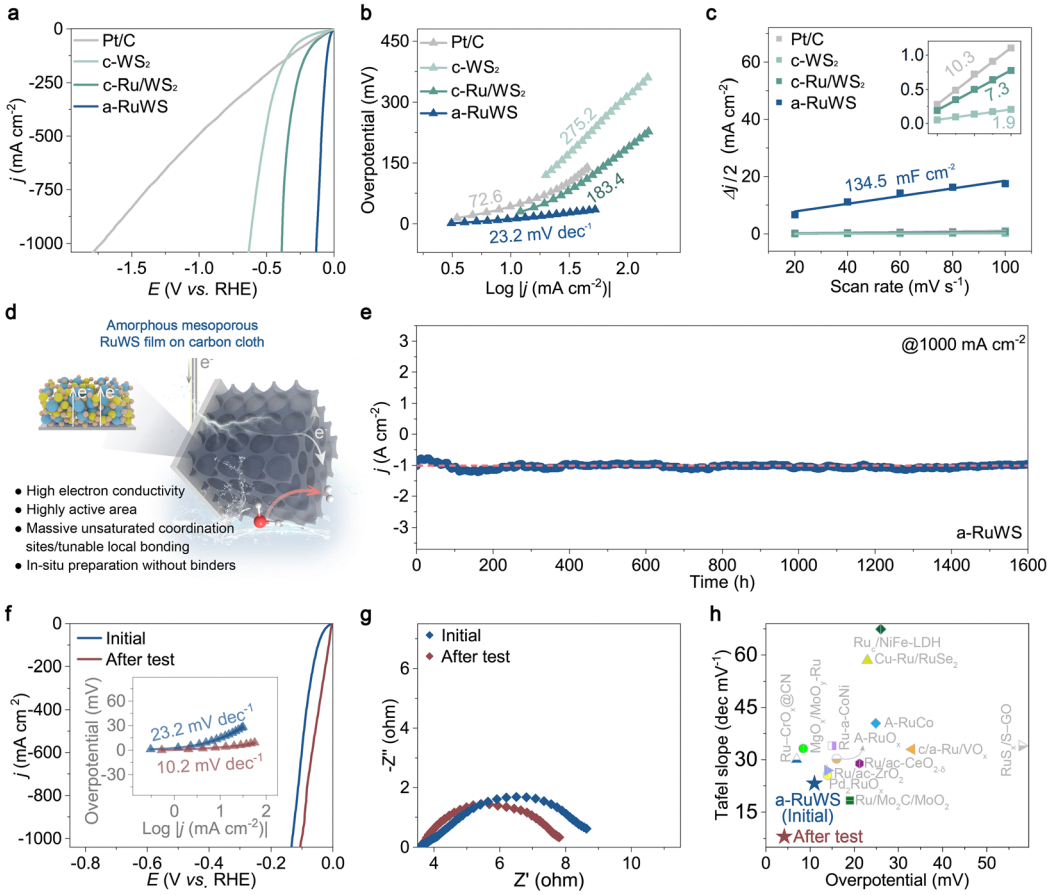

Fig. 4 Electrocatalytic performance of amorphous mesoporous RuWS film. (a) HER linear sweep voltammetry (LSV) curves with *iR*-correction, (b) Tafel slopes for HER, and (c) plots of current density *versus* scan rate of commercial Pt/C, crystalline WS_2 (denoted as c-WS_2), crystalline WS_2 with Ru nanoparticles (denoted as c-Ru/WS_2), and amorphous mesoporous RuWS film (denoted as a-RuWS) in an aqueous solution of 1.0 M KOH. (d) Schematic illustration of the advantageous catalytic environment of amorphous mesoporous RuWS film on carbon cloth. (e) Chronoamperometry curves of amorphous mesoporous RuWS film at 1000 mA cm^{-2}. (f) LSV curves and Tafel slopes (inset) and (g) EIS Nyquist plots of amorphous mesoporous RuWS film before and after the HER stability test. (h) Comparison of overpotential and Tafel slope with those of other reported amorphous/Ru-based HER electrocatalysts.

membrane water electrolyzer (AEMWE) was assembled using the amorphous mesoporous RuWS film as the cathode and commercial IrO_2 as the anode to further evaluate the practical application potential (Fig. S43a). The assembled AEMWE exhibited a low cell voltage of 1.60 V at a current density of 1.0 A cm^{-2} and showed no obvious performance degradation during continuous operation for 27 h, confirming favorable potential for practical water electrolysis (Fig. S43b and c).

Electrochemical reconfiguration of amorphous mesoporous RuWS film

To investigate the mechanistic origin of the long-term stability and performance enhancement of the amorphous mesoporous RuWS film, we systematically monitored the dynamic evolution of the atomic/electronic structure under an applied negative electric field (Fig. 5a). Uniformly distributed sub-nanometer clusters emerged on the mesoporous film and gradually evolved into nanoparticles (Fig. S44). AC-HAADF-STEM imaging revealed the expansion of crystalline domains in the amorphous matrix and the eventual formation of large-area crystalline phases. The resulting crystalline region showed distinct wide lattice stripes (0.677 nm) corresponding to WS_2 (Fig. S45) and clear tetragonal lattice arrangements for 1T-phase (Fig. 5b and c). The intensity distribution map of the blue lines specifically revealed two sulfur atoms between the neighboring tungsten atoms, indicating an octahedral-coordinated 1T-phase atomic pattern[42] (W–S–S–W; Fig. 5c and e). Notably, a considerable number of atomic-level dark spots were detected on the WS_2 crystal (Fig. 5d, marked with yellow circles), which could be ascribed to the doping of Ru atoms. The corresponding HAADF intensity line profiles further confirmed the existence of Ru single atoms (Fig. 5e and Fig. S46). The XANES spectrum at the Ru K-edge showed a slightly higher absorption edge for the post-test sample, indicating an increased oxidation state of Ru element (Fig. S47). EXAFS spectra exhibited a prominent peak at 1.52 Å corresponding to the Ru–S scattering feature and thus confirming the isolated dispersion of Ru atoms (Fig. 5f). Compared with 2H-phase WS_2,

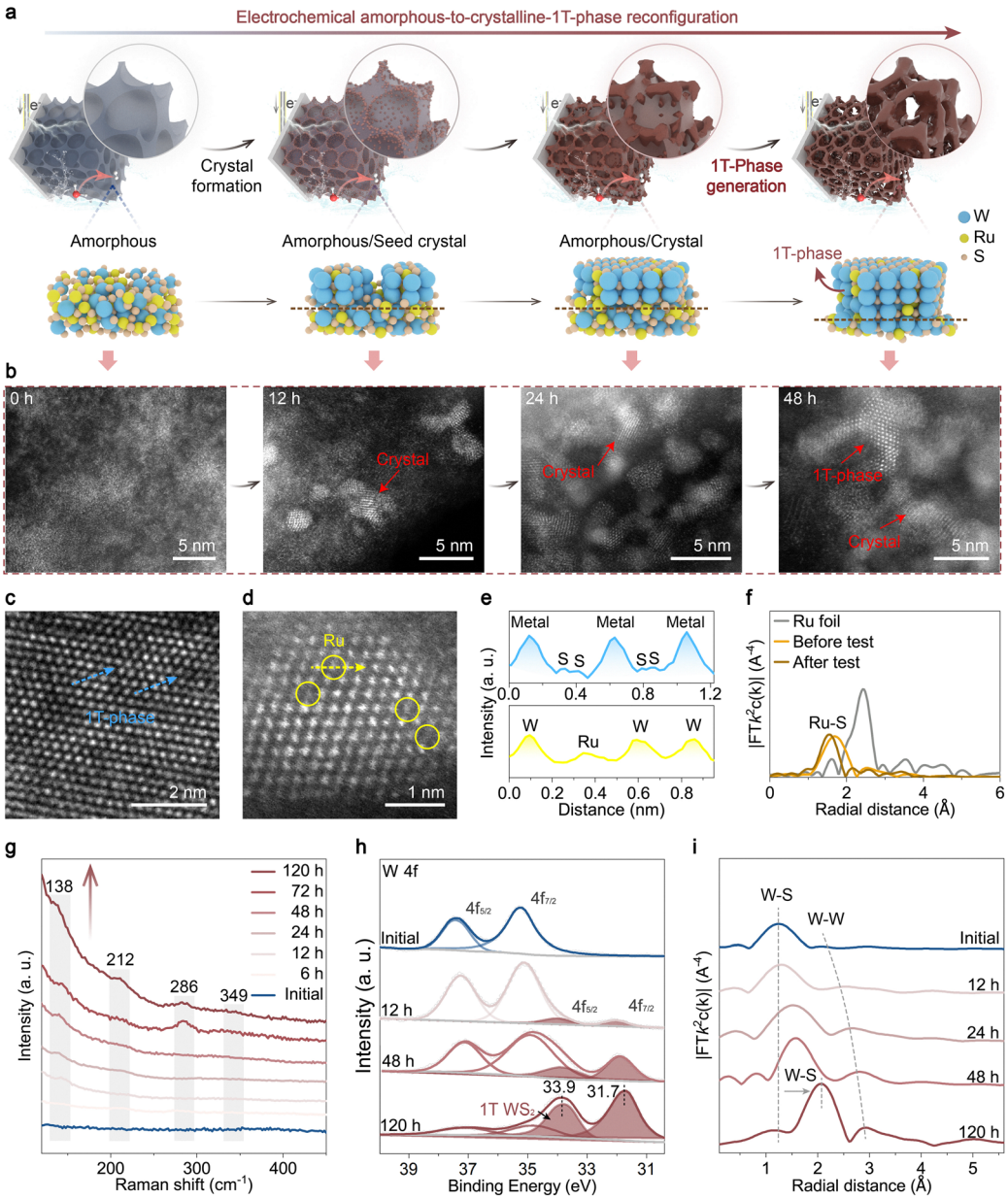

Fig. 5 Reconfiguration of amorphous mesoporous RuWS film during the electrochemical process. (a) Schematic illustration of gradual formation of crystalline nuclei from amorphous mesoporous RuWS film during the electrochemical process, followed by the ultimate generation of crystalline Ru–W bimetallic sulfide with 1T-phase. (b) AC-HAADF-STEM images of generation from amorphous mesoporous RuWS film during the electrochemical test. (c) HRTEM and (d) AC-HAADF-STEM images of amorphous mesoporous RuWS film after electrochemical test. (e) Atomic arrangement profiles along the marked lines in (c) and (d). (f) EXAFS spectra at the Ru K-edge of amorphous mesoporous RuWS film before and after the electrochemical test. (g) Raman spectra, (h) high-resolution XPS spectra of W 4f and (i) EXAFS spectra at W L_3-edge of amorphous mesoporous RuWS film at various periods of the electrochemical test.

the characteristic (002) peak of the reconstructed 1T-phase exhibited a distinct negative shift, indicating that the introduction of Ru increased the interlayer spacing[49] (Fig. S48). The positively shifted Ru 3p XPS signal further indicated an elevated valence state of Ru (Fig. S49a). Meanwhile, the negative shift of the S 2p signals implied that the Ru atoms probably possessed a positive valence state *via* the association with S atoms in the WS_2 matrix (Fig. S49b).

In addition, Raman spectroscopy revealed progressively intensified peaks of 1T WS_2 at 138, 212, 286, and 349 cm^{-1} with increasing testing time, indicating a growing fraction of the 1T-phase[42,49] (Fig. 5g). The W 4f XPS spectrum exhibited two new peaks at 31.7 and 33.9 eV after testing, approximately 0.9 eV lower than the corresponding peaks for 2H WS_2, which can be attributed to the formation of 1T WS_2[37] (Fig. 5h and Fig. S35e). Accordingly, the content of converted 1T-phase estimated from integrated peak areas reached 82.7% at 120 h (Table S3). Meanwhile, the EXAFS spectra evolved as a function of time, featuring the emergence and intensification of a new peak, attributed to W–W coordination (Fig. 5i). The

concomitant elongation of both W–S and W–W bonds to 2.04 and 2.87 Å, respectively, was consistent with the structural characteristics of 1T WS_2,[37,56,57] further implying the atomic reconstruction during the electrocatalytic test (Fig. 5i and Fig. S50–S53, Table S4).

Mechanism for electrochemical amorphous-to-crystalline-1T-phase reconfiguration

First-principles calculations were performed to elucidate the atomic-level mechanism for the electrochemically induced reconfiguration[56,58,59] (Fig. 6). Three structural models of the amorphous Ru–W sulfide phase featuring a sulfur-bridged network of metal atoms with coordination-unsaturated W and S sites, namely amorphous RuWS-1, RuWS-2 and RuWS-3, were constructed and geometrically stabilized through structure optimization (Fig. 6a). To reduce the calculation complexity, only one Ru atom was involved in each model. Taking the standard structure of 1T-phase Ru–WS_2 as the baseline state, the atomic disorder increases progressively from amorphous RuWS-1 to RuWS-3 with consistent atom number and element species, corresponding to a gradual rise in structural free energy. The energy trend indicates a thermodynamic driving force for the conversion from the disordered amorphous states toward 1T-phase Ru–WS_2.

However, both theoretical analysis and experimental observation show that the amorphous configurations are locally stable. This implies that the transformation is kinetically hindered, therefore requiring a substantial external driving force to proceed at an appreciable rate. To mimic the electrochemical environment presented in HER, further calculations were performed on the amorphous Ru–W sulfide models with additional electrons to simulate the effect of an applied negative potential. Interestingly, all of these three structures undergo atomic coordination and ordered rearrangement following the electron injection, resulting in the formation of 1T-phase Ru–WS_2 (Fig. 6c and Fig. S54). In particular, amorphous RuWS-1 requires only one electron for shifting from a disordered atomic arrangement to an ordered 1T-phase, whereas amorphous RuWS-2 and amorphous RuWS-3 necessitate the addition of two and four electrons, respectively. It is worth noting that the number of injected external electrons required for the structural evolution is related to the free energy of the amorphous structures, which intrinsically depends on the degree of atomic disorder (Fig. 6b). This suggests an electrochemically driven mechanism for structural reorganization in the amorphous Ru–W bimetallic sulfide, triggering directional construction of its metastable crystalline phase by satisfying the electronic requirements. This is consistent with the electrocatalytic stability results at different applied potentials.

To further explore the influence of catalyst structure in this reconfiguration, disordered atomic configurations of amorphous WS_x with metal network (denoted as amorphous WS_x) as well as amorphous Ru–W bimetallic sulfide with the presence of Ru–W and W-W bonds (denoted as amorphous RuWS-4) were constructed and fully optimized by selectively replacing Ru and S with W atoms in amorphous RuWS-3, respectively (Fig. 6d, e and Fig. S55). Notably, after injecting four electrons into each geometrically optimized structure, the former achieved an ordered rearrangement to form an atomic configuration of 1T WS_2, while the latter remained in a disordered state. It seems that the establishment of sulfur-bridged metal networks within the disordered structure is crucial for the amorphous to metastable crystalline phase reconfiguration under electrochemical induction. In addition, sulfur-bridged amorphous RuMoS also undergoes atomic rearrangement upon electron injection, further highlighting the critical role of such bridging motifs during the reconstruction (Fig. S56). As visualized in the electron localization functions for the stabilized amorphous RuWS-3 (Fig. 6f), an obvious electron delocalization effect is observed around the structure defects. Accompanying electron injection, external electrons in amorphous RuWS-3 are more localized at the structure defects to promote the reconfiguration, and thus producing an ordered rearrangement of the local electron density (Figs. S57–S59). The structural reconfiguration of amorphous WS_x aligns with the above results, while amorphous RuWS-4 exhibits more serious electron redistribution. It primarily stems from the coexisting metal–metal and metal–sulfide bonds, whose inherent disparity drives irregular transfer of electrons (Fig. S60 and S61).

Furthermore, Bader charges among atoms in amorphous RuWS-1, amorphous RuWS-2, amorphous RuWS-3, and amorphous WS_x all redistribute upon electron injection. These demonstrate that the enhanced interatomic interactions originated from the electron transfer, thereby driving the reconfiguration of these disordered structures into the crystalline 1T-phase (Fig. 6g and Fig. S62–S64). The increased electron loss in the metallic atoms and the enhanced electron capture ability of S atoms reveal that the electrons transfer directionally from the metal center to the bridging S atoms (Fig. S62). Such a result is consistent with the distinct negative shift of the peak in the S 2p XPS spectrum (Fig. S49b). It implies that the electron transfer between metal and S atoms in the disordered structures exhibits a ''metal to sulfur'' polarity in the bonding. Such enhanced polarization effect promotes the bonding strength of metal–sulfur bonds,[57] thereby readily stimulating new bond formation. In the pristine structure, the substantial charge disparity between defect-site S atoms and fully coordinated S atoms is alleviated after electronic injection, leading to a more uniform distribution of electrons on the sulfur atoms (Fig. 6g and Fig. S62–S64). In contrast, such equilibration of electron distribution is suppressed in amorphous RuWS-4 due to the presence of metallic Ru–Ru and W–W bonds (Fig. S65). These observations confirm that the bridging effect of sulfur atoms enables the metal network to achieve efficient interatomic cooperative charge redistribution, ensuring the structural stability for metastable crystalline phase during the atomic rearrangement. Statistical analysis of bond length distributions before and after electron injection in amorphous RuWS-1, amorphous RuWS-2 and amorphous RuWS-3 shows that the length distribution of the W–S bond in the reconstructed 1T-phase Ru–WS_2 has approximately

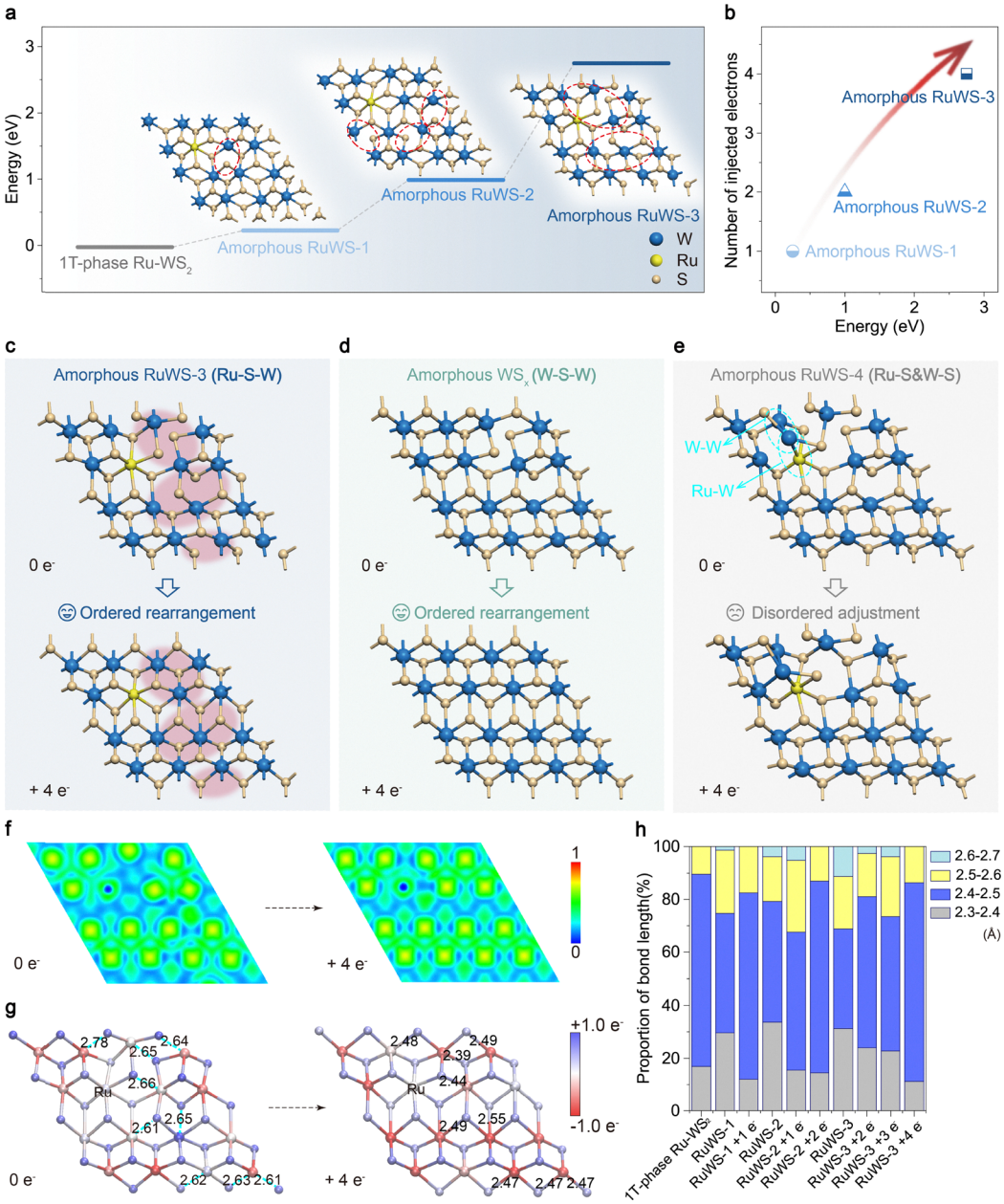

Fig. 6 Mechanism investigation of electrochemical amorphous-to-crystalline reconfiguration. (a) Free energies of three disordered configurations of amorphous Ru–W bimetallic composites with increasing atomic disorder, referenced to the standard 1T-phase Ru–WS_2 as the baseline state. (b) Number of injected electrons required for the reconfiguration. (c)–(e) Atomic configurations of (c) amorphous RuWS-3, (d) amorphous WS_x, and (e) amorphous RuWS-4 before and after being injected with 4 electrons. (f) Variation of electron localization function before and after being injected with 4 electrons in amorphous RuWS-3. The red and blue areas represent electron localization and delocalization, respectively. (g) Bader charge on amorphous RuWS-3 and relevant bond lengths before and after the injection of 4 electrons. Red represents lost electrons, and blue represents gained electrons. The unit of bond length is angstrom (Å). (h) Proportion of bonds with different lengths in various structures.

70% of bonds falling within the 2.4–2.5 Å range, with no bonds exceeding 2.6 Å. This is extremely similar to the standard 1T-phase Ru–WS_2 structure (Fig. 6h), further confirming the generation of metastable crystalline 1T-phases relying on electrocatalytic structural reconfiguration. Indeed, the Ru–S bond length remains largely unchanged before and after reconfiguration, maintaining an average value of 2.6 Å (Table S5).

Conclusions

In summary, we have employed a micellar film system to prepare large-area mesoporous films of amorphous bimetal sulfide through hierarchical "pyridyl–Ru^{3+}–WS_4^{2-}" coordination and retarded crystallization. Such amorphous materials revealed excellent HER performance and long-term stability. Interestingly, the electrochemical process induced an

"amorphous-to-crystalline" transition and eventually generated crystalline Ru–W bimetallic sulfide with a thermodynamically metastable but electrochemically more favored 1T-phase. Theoretical calculations demonstrated that the reconfiguration is triggered by sufficient electron injection, and the sulfur-bridged metallic network creates rapid charge transfer pathways to ensure the stable maintenance of the reconfigured 1T-phase. Notably, the reconfigured catalyst formed after a 1600-h electrochemical test revealed a remarkably reduced overpotential of only 4 mV at a current density of 10 mA cm^{-2}. Overall, this work not only provides an innovative route to functional amorphous composites, especially with a mesoporous film feature, but also establishes a novel paradigm for phase engineering toward highly active electrocatalysts, aiming at advanced sustainable energy conversion technologies.

Author contributions

J.W. designed and conducted the experiments, performed the catalyst preparation, characterization and catalytic tests, analyzed the data and wrote the paper. Y.S. supervised the experiments. Y.Z. and X.Y. conducted the writing review. X.Y. and H.T. performed the DFT calculations. C.L. and H.Q. supervised the project and revised the paper. All the authors discussed the results and commented on the paper.

Conflicts of interest

There are no conflicts to declare.

Data availability

The data supporting this article have been included as part of the supplementary information (SI). Supplementary information: detailed experimental procedures, supplementary characterizations as well as additional data. See DOI: https://doi.org/10.1039/d6ey00096g.

Acknowledgements

We are grateful for financial support from the National Natural Science Foundation of China (22425203, 22502117) and the Innovation Program of Shanghai Municipal Education Commission (202101070002E00084). This work was also supported by BL13SSW and the User Experiment Assist System of Shanghai Synchrotron Radiation Facility (SSRF).

Notes and references

1 S. Lan, L. Zhu, Z. Wu, L. Gu, Q. Zhang, H. Kong, J. Liu, R. Song, S. Liu, G. Sha, Y. Wang, Q. Liu, W. Liu, P. Wang, C.-T. Liu, Y. Ren and X.-L. Wang, *Nat. Mater.*, 2021, **20**, 1347–1352.
2 Y. Liu, A. Madanchi, A. S. Anker, L. Simine and V. L. Deringer, *Nat. Rev. Mater.*, 2024, **10**, 228–241.
3 J. Zhang, L. Xu, X. Yang, S. Guo, Y. Zhang, Y. Zhao, G. Wu and G. Li, *Angew. Chem., Int. Ed.*, 2024, **63**, e202405641.
4 C. Pei, S. Chen, T. Zhao, M. Li, Z. Cui, B. Sun, S. Hu, S. Lan, H. Hahn and T. Feng, *Adv. Mater.*, 2022, **34**, 2200850.
5 Z. Su, X. Chen, M. Sun, X. Yang, J. Kang, Z. Cai and L. Guo, *Angew. Chem., Int. Ed.*, 2024, **64**, e202416878.
6 J. Wang, L. Zhao, Y. Zou, J. Dai, Q. Zheng, X. Zou, L. Hu, W. Hou, R. Wang, K. Wang, Y. Shi, G. Zhan, Y. Yao and L. Zhang, *J. Am. Chem. Soc.*, 2024, **146**, 11152–11163.
7 F. Feng, C. Ma, S. Han, X. Ma, C. He, H. Zhang, W. Cao, X. Meng, J. Xia, L. Zhu, Y. Tian, Q. Wang, Q. Yun and Q. Lu, *Angew. Chem., Int. Ed.*, 2024, **63**, e202405173.
8 Y. Mu, D. Zhang, T. Gao, L. Wang, L. Zhang, X. Zou, W. Zheng, J. Fan and X. Cui, *Angew. Chem., Int. Ed.*, 2025, **64**, e202505908.
9 C. Wan, Z. Zhang, J. Dong, M. Xu, H. Pu, D. Baumann, Z. Lin, S. Wang, J. Huang, A. H. Shah, X. Pan, T. Hu, A. N. Alexandrova, Y. Huang and X. Duan, *Nat. Mater.*, 2023, **22**, 1022–1029.
10 E. Shin, D.-H. Kim, M. Sagong, J. Choe, S. H. Park, J. Ahn, J. W. Baek, M. Kim, S. Woo, Y. Cho, S.-J. Choi, S.-J. Kim, J. M. Yuk, J. Li, S.-Y. Choi and I. D. Kim, *Adv. Mater.*, 2025, **37**, 2419790.
11 D. Zhang, F. Wang, W. Zhao, M. Cui, X. Fan, R. Liang, Q. Ou and S. Zhang, *Adv. Sci.*, 2022, **9**, 2202445.
12 Y. Li, Q. Yin, B. Jia, H. Wang, H. Gu, Q. Hu, H. Yang, T. Guo, P. Hu, L. Li, L. M. Liu and L. Guo, *Angew. Chem., Int. Ed.*, 2025, **64**, e202505668.
13 J. A. Bau, A.-H. Emwas, P. Nikolaienko, A. A. Aljarb, V. Tung and M. Rueping, *Nat. Catal.*, 2022, **5**, 397–404.
14 J. Staszak-Jirkovský, Christos D. Malliakas, Pietro P. Lopes, N. Danilovic, Subrahmanyam S. Kota, K.-C. Chang, B. Genorio, D. Strmcnik, Vojislav R. Stamenkovic, M. G. Kanatzidis and N. M. Markovic, *Nat. Mater.*, 2015, **15**, 197–203.
15 W. Ding, D. Ji, K. Wang, Y. Li, Q. Luo, R. Wang, L. Li, X. Qin and S. Peng, *Angew. Chem., Int. Ed.*, 2024, **64**, e202418640.
16 J. Liu and L. Guo, *Matter*, 2021, **4**, 2850–2873.
17 G. Chen, Z. Hu, Y. Zhu, B. Gu, Y. Zhong, H. J. Lin, C. T. Chen, W. Zhou and Z. Shao, *Adv. Mater.*, 2018, **30**, 1804333.
18 Y. Yue, X. Zhong, M. Sun, J. Du, W. Gao, W. Hu, C. Zhao, J. Li, B. Huang, Z. Li and C. Li, *Adv. Mater.*, 2025, 2418058.
19 X.-Y. Zhang, S.-S. Yu, J.-J. Chen, K. Gao, H.-Q. Yu and Y. Yu, *Adv. Mater.*, 2025, **37**, 2419050.
20 M. Liu, H. Su, X. Liu, X. He, P. Tan, F. Liu and J. Pan, *Nat. Commun.*, 2025, **16**, 2826.
21 J. Nie, J. Shi, L. Li, M. Y. Xie, Z. Y. Ouyang, M. H. Xian, G. F. Huang, H. Wan, W. Hu and W. Q. Huang, *Adv. Energy Mater.*, 2024, **15**, 2404246.
22 W. Bao, J. Liu, T. Ai, J. Han, J. Hou, W. Li, X. Wei, X. Zou, Z. Deng and J. Zhang, *Adv. Funct. Mater.*, 2024, **34**, 2408364.
23 Y. Duan, Z. Y. Yu, S. J. Hu, X. S. Zheng, C. T. Zhang, H. H. Ding, B. C. Hu, Q. Q. Fu, Z. L. Yu, X. Zheng, J. F. Zhu, M. R. Gao and S. H. Yu, *Angew. Chem., Int. Ed.*, 2019, **58**, 15772–15777.

24 J. Sun, S. Zhou, Z. Zhao, S. Qin, X. Meng, C.-H. Tung and L.-Z. Wu, *Energy Environ. Sci.*, 2025, **18**, 1952–1962.
25 Q. Fu, L. W. Wong, F. Zheng, X. Zheng, C. S. Tsang, K. H. Lai, W. Shen, T. H. Ly, Q. Deng and J. Zhao, *Nat. Commun.*, 2023, **14**, 6462.
26 X. Ding, D. Liu, P. Zhao, X. Chen, H. Wang, F. E. Oropeza, G. Gorni, M. Barawi, M. García-Tecedor, V. A. de la Peña O'Shea, J. P. Hofmann, J. Li, J. Kim, S. Cho, R. Wu and K. H. L. Zhang, *Nat. Commun.*, 2024, **15**, 5336.
27 Y. Yao, G. Zhao, X. Guo, P. Xiong, Z. Xu, L. Zhang, C. Chen, C. Xu, T.-S. Wu, Y.-L. Soo, Z. Cui, M. M.-J. Li and Y. Zhu, *J. Am. Chem. Soc.*, 2024, **146**, 15219–15229.
28 J. Sang, P. Wei, T. Liu, H. Lv, X. Ni, D. Gao, J. Zhang, H. Li, Y. Zang, F. Yang, Z. Liu, G. Wang and X. Bao, *Angew. Chem., Int. Ed.*, 2021, **61**, e202114238.
29 P. Tian, W. Zong, J. Xiong, W. Liu, J. Liu, Y. Dai, J. Zhu, S. Huang, S. Song, K. Chu, G. He and N. Han, *Adv. Funct. Mater.*, 2025, **5**, 2504862.
30 J. Feng, X. Wang and H. Pan, *Adv. Mater.*, 2024, **36**, 2411688.
31 B. Lu, C. Wahl, R. dos Reis, J. Edgington, X. K. Lu, R. Li, M. E. Sweers, B. Ruggiero, G. T. K. K. Gunasooriya, V. Dravid and L. C. Seitz, *Nat. Catal.*, 2024, **7**, 868–877.
32 L. Wang, Y. Hao, L. Deng, F. Hu, S. Zhao, L. Li and S. Peng, *Nat. Commun.*, 2022, **13**, 5785.
33 J. T. Mefford, A. R. Akbashev, M. Kang, C. L. Bentley, W. E. Gent, H. D. Deng, D. H. Alsem, Y.-S. Yu, N. J. Salmon, D. A. Shapiro, P. R. Unwin and W. C. Chueh, *Nature*, 2021, **593**, 67–73.
34 J.-W. Zhao, H.-Y. Wang, L. Feng, J.-Z. Zhu, J.-X. Liu and W.-X. Li, *Chem. Rev.*, 2023, **124**, 164–209.
35 J. Zhou, J. Lin, X. Huang, Y. Zhou, Y. Chen, J. Xia, H. Wang, Y. Xie, H. Yu, J. Lei, D. Wu, F. Liu, Q. Fu, Q. Zeng, C.-H. Hsu, C. Yang, L. Lu, T. Yu, Z. Shen, H. Lin, B. I. Yakobson, Q. Liu, K. Suenaga, G. Liu and Z. Liu, *Nature*, 2018, **556**, 355–359.
36 W. Zhai, J. Qi, C. Xu, B. Chen, Z. Li, Y. Wang, L. Zhai, Y. Yao, S. Li, Q. Zhang, Y. Ge, B. Chi, Y. Ren, Z. Huang, Z. Lai, L. Gu, Y. Zhu, Q. He and H. Zhang, *J. Am. Chem. Soc.*, 2023, **145**, 13444–13451.
37 Z. Li, L. Zhai, Q. Zhang, W. Zhai, P. Li, B. Chen, C. Chen, Y. Yao, Y. Ge, H. Yang, P. Qiao, J. Kang, Z. Shi, A. Zhang, H. Wang, J. Liang, J. Liu, Z. Guan, L. Liao, V. A. Neacsu, C. Ma, Y. Chen, Y. Zhu, C.-S. Lee, L. Ma, Y. Du, L. Gu, J.-F. Li, Z.-Q. Tian, F. Ding and H. Zhang, *Nat. Mater.*, 2024, **23**, 1355–1362.
38 Q. Gao, H. Chen, W.-S. Lu, Y.-H. Chan, Z. Chen, Y. Huang, Z. Liu and P. Chen, *Nat. Commun.*, 2025, **16**, 3784.
39 Z. Lai, Q. He, T. H. Tran, D. V. M. Repaka, D.-D. Zhou, Y. Sun, S. Xi, Y. Li, A. Chaturvedi, C. Tan, B. Chen, G.-H. Nam, B. Li, C. Ling, W. Zhai, Z. Shi, D. Hu, V. Sharma, Z. Hu, Y. Chen, Z. Zhang, Y. Yu, X. Renshaw Wang, R. V. Ramanujan, Y. Ma, K. Hippalgaonkar and H. Zhang, *Nat. Mater.*, 2021, **20**, 1113–1120.
40 R. Yang, L. Mei, Q. Zhang, Y. Fan, H. S. Shin, D. Voiry and Z. Zeng, *Nat. Protoc.*, 2022, **17**, 358–377.
41 R. Yang, L. Mei, Z. Lin, Y. Fan, J. Lim, J. Guo, Y. Liu, H. S. Shin, D. Voiry, Q. Lu, J. Li and Z. Zeng, *Nat. Rev. Chem.*, 2024, **8**, 410–432.
42 A. Han, X. Zhou, X. Wang, S. Liu, Q. Xiong, Q. Zhang, L. Gu, Z. Zhuang, W. Zhang, F. Li, D. Wang, L.-J. Li and Y. Li, *Nat. Commun.*, 2021, **12**, 709.
43 L. Xie, L. Wang, X. Liu, J. Chen, X. Wen, W. Zhao, S. Liu and Q. Zhao, *Nat. Commun.*, 2024, **15**, 5702.
44 B. Zhou, J. Zhou, L. Wang, J. H. Kang, A. Zhang, J. Zhou, D. Zhang, D. Xu, B. Hu, S. Deng, L. Huang, C. W. Wong, Y. Huang and X. Duan, *Nat. Synth.*, 2023, **3**, 67–75.
45 J. Wu, Z. Chen, K. Yang, X. Zhou, H. Li, Z. Wang, M. Su, R. Zhang, T. Wang, Q. Hu, N. Yan, C. Liu, B. Zhang, M. Yang, S. Xi and K. P. Loh, *Nat. Nanotechnol.*, 2025, **20**, 1043–1051.
46 L. Mei, Z. Gao, R. Yang, Z. Zhang, M. Sun, X. Liang, Y. Zhang, T. Ying, H. Hu, D. Li, Q. Zhang, M. D. Gu, L. Gu, J. Zhou, B. Huang, D. Voiry, X. C. Zeng, Y. Chai, J. Li, X. Yu and Z. Zeng, *Nat. Synth.*, 2024, **4**, 303–313.
47 T. Gao, J. Gu, C. Yang, R. Wang, C. Wang, P. Zhang, J. Li, X. Zheng, Y. Fan, P. Yang, X. Hua, J. Hui and H. Zhang, *J. Am. Chem. Soc.*, 2025, **147**, 25385–25396.
48 W. Hou, A. Azizimanesh, A. Dey, Y. Yang, W. Wang, C. Shao, H. Wu, H. Askari, S. Singh and S. M. Wu, *Nat. Electron.*, 2023, **7**, 8–16.
49 Y. Sun, Y. Zang, W. Tian, X. Yu, J. Qi, L. Chen, X. Liu and H. Qiu, *Energy Environ. Sci.*, 2022, **15**, 1201–1210.
50 Y. He, L. Liu, C. Zhu, S. Guo, P. Golani, B. Koo, P. Tang, Z. Zhao, M. Xu, C. Zhu, P. Yu, X. Zhou, C. Gao, X. Wang, Z. Shi, L. Zheng, J. Yang, B. Shin, J. Arbiol, H. Duan, Y. Du, M. Heggen, R. E. Dunin-Borkowski, W. Guo, Q. J. Wang, Z. Zhang and Z. Liu, *Nat. Catal.*, 2022, **5**, 212–221.
51 X. Wang, B. Liu, S. Ma, Y. Zhang, L. Wang, G. Zhu, W. Huang and S. Wang, *Nat. Commun.*, 2024, **15**, 2600.
52 Z. Shi, W. Qin, Z. Hu, M. Ma, H. Liu, Z. Shu, Y. Jiang, H. Xia, W. Shi, C. Y. Zhang, X. Sang, C. Guo, Y. Li, C. Liu, C. Gong, H. Wang, S. Liu, L. Tapasztó, C. Gao, F. Liu, P. Tang, Y. Liu, H. Duan, E. Xie, Z. Zhang, Z. Liu and Y. He, *Nat. Mater.*, 2025, **24**, 1186–1194.
53 J. Wang, Y. Sun, Y. Cui and H. Qiu, *Energy Environ. Sci.*, 2025, **18**, 1756–1766.
54 Y. Kang, S. Li, O. Cretu, K. Kimoto, Y. Zhao, L. Zhu, X. Wei, L. Fu, D. Jiang, C. Wan, B. Jiang, T. Asahi, D. Zhang, H. Li and Y. Yamauchi, *Sci. Adv.*, 2024, **10**, eado2442.
55 B. Wu, X. Liu, P. Liu, G. Wu, L. Tian, X. Han, J. Li and X. Hong, *Nat. Synth.*, 2025, **4**, 370–379.
56 Z. Chen, J.-a. Shi, J. Huang, Y. Chang, R. Xu, K. Xu, X. Zhang, X. Liu, D. Tian, Y. Zhang, S. Ali, X. Dai, G. Liu, Z. Dai, S. Zhang, F. Fei, X. Xi, Y. Hao, L. He, W. Zhou, T. Yang, J. Gao, F. Ding, Y. Xu, F. Song, B. Jin, X. Wang, Y. Shi, R. Zhang and X. Wang, *Nat. Mater.*, 2026, **25**, 573–580.
57 Z. Li, H. Yang, M. Sun, A. Zhang, Y. Ge, X. Long, B. Huang, L. Zhai, W. Zhai, L. Li, L. Wang, C. Wang, Y. Xu, Y. Cai, P. Liu, B. Chen, L. Gu, P. Qiao, Q. Zhang, F. Ding and H. Zhang, *J. Am. Chem. Soc.*, 2026, **148**, 7342–7354.
58 S. Zha, C. Lin and T. S. Choksi, *ACS Catal.*, 2026, **16**, 6098–6121.
59 A. Das, B. K. Das and K. K. Chattopadhyay, *Comput. Mater. Sci.*, 2023, **229**, 112418.